The Astrophysical Journal, 923:243 (13pp), 2021 December 20 https://doi.org/10.3847/1538-4357/ac2738

Swift/XRT Deep Galactic Plane Survey Discovery of a New Intermediate Polar Cataclysmic Variable, Swift J183920.1-045350

Nicholas M. Gorgone[1,2], Patrick A. Woudt[3], David Buckley[4], Koji Mukai[5,6], Chryssa Kouveliotou[1,2], Daniela Huppenkothen[7], Ersin Göğüş[8], Eric Bellm[9], Justin D. Linford[10], Alexander J. van der Horst[1,2], Matthew G. Baring[11], Dieter Hartmann[12], Paul Barrett[1], Bradley Cenko[13,14], Melissa Graham[9], Johnathan Granot[1,15], Fiona Harrison[16], Jamie Kennea[17], Brendan M. O'Connor[1,2], Stephen Potter[4], Daniel Stern[18], Patrick Slane[19], and Ralph Wijers[20]

[1] Department of Physics, The George Washington University, Washington, DC 20052, USA; nicholas.gorgone@gmail.com
[2] Astronomy, Physics and Statistics Institute of Sciences (APSIS), The George Washington University, Washington, DC 20052, USA
[3] Department of Astronomy, University of Cape Town, Private Bag X3, Rondebosch 7701, South Africa
[4] South African Astronomical Observatory, P.O. Box 9, 7935 Observatory, South Africa
[5] CRESST II and X-ray Astrophysics Laboratory, NASA/GSFC, Greenbelt, MD 20771, USA
[6] Department of Physics, University of Maryland Baltimore County, 1000 Hilltop Circle, Baltimore MD 21250, USA
[7] SRON Netherlands Institute for Space Research, Sorbonnelaan 2, 3584 CA, Utrecht, The Netherlands
[8] Sabancı University, Faculty of Engineering and Natural Sciences, İstanbul 34956, Turkey
[9] DIRAC Institute, Department of Astronomy, University of Washington, 3910 15th Avenue NE, Seattle, WA 98195, USA
[10] National Radio Astronomy Observatory, P.O. Box O, Socorro, NM 87801, USA
[11] Department of Physics and Astronomy—MS 108, Rice University, 6100 Main Street, Houston, Texas 77251-1892, USA
[12] Department of Physics and Astronomy, Clemson University, Kinard Lab of Physics, Clemson, SC 29634-0978, USA
[13] Astrophysics Science Division, NASA Goddard Space Flight Center, MC 661, Greenbelt, MD 20771, USA
[14] Joint Space-Science Institute, University of Maryland, College Park, MD 20742, USA
[15] Department of Natural Sciences, The Open University of Israel, P.O. Box 808, Ra'anana 43537, Israel
[16] Cahill Center for Astrophysics, California Institute of Technology, 1216 East California Boulevard, Pasadena, CA 91125, USA
[17] Department of Astronomy and Astrophysics, The Pennsylvania State University, 525 Davey Lab, University Park, PA 16802, USA
[18] Jet Propulsion Laboratory, California Institute of Technology, 4800 Oak Grove Drive, Mail Stop 169-221, Pasadena, CA 91109, USA
[19] Center for Astrophysics, Harvard & Smithsonian, 60 Garden St., Cambridge, MA 02138, USA
[20] University of Amsterdam, Science Park 904, 1098 XH Amsterdam, The Netherlands
Received 2021 April 10; revised 2021 September 10; accepted 2021 September 14; published 2021 December 24

Abstract

We report on the Swift/XRT Deep Galactic Plane Survey discovery and multiwavelength follow-up observations of a new intermediate polar (IP) cataclysmic variable, Swift J183920.1-045350. A 449.7 s spin period is found in XMM-Newton and NuSTAR data, accompanied by a 459.9 s optical period that is most likely the synodic, or beat period, produced from a 5.6 hr orbital period. The orbital period is seen with moderate significance in independent long-baseline optical photometry observations taken with the ZTF and SAAO telescopes. We find that the X-ray pulse fraction of the source decreases with increasing energy. The X-ray spectra are consistent with the presence of an Fe emission line complex with both local and interstellar absorption. In the optical spectra, strong Hα, H I, He I, and He II emission lines are observed, all common features in magnetic CVs. The source properties are thus typical of known IPs, with the exception of its estimated distance of $2.26^{+1.93}_{-0.83}$ kpc, which is larger than typical, extending the reach of the CV population in our Galaxy.

Unified Astronomy Thesaurus concepts: Cataclysmic variable stars (203); DQ Herculis stars (407)

1. Introduction

Cataclysmic variables (CVs) are binary systems, including a white dwarf (WD) accreting material from a companion, usually a main-sequence star, which is undergoing Roche Lobe overflow. An accretion disk can form if the magnetic field of the primary (the WD) is sufficiently small, i.e., $B \lesssim 10^6$ G (see, e.g., Warner 1992, 1995; Coppejans 2016). Systems with field strengths below this threshold are known as nonmagnetic CVs, whereas the magnetic systems exceeding this field strength are divided into polars and intermediate polars (IPs). The difference between the latter two categories is that in the most magnetic WDs (polars), the Alfvén radius (R_A) extends to the L1 Lagrange point, which stops an accretion disk from forming, while in the lower B-field IPs an accretion disk can form between L1 and R_A. In addition, the magnetic field of polars induces a torque that approximately synchronizes the WD spins to their orbital periods. In contrast, in IPs the weaker WD fields cannot synchronize spins with orbital periods and the WDs are in fact spun up by accretion torques (Cropper 1990; Patterson 1994; Wickramasinghe 2014).

In IPs, material at the inner edge of the disk is funnelled along the magnetic field lines toward the poles of the WD, forming a shock in the accretion column as it interacts with the WD atmosphere. Accretion from the inner edge of the disk results in azimuthally extended accretion curtains, akin to the auroral zones on Earth. During accretion, several emission mechanisms are at play; for a comprehensive review, see Mukai (2017). At the shock front, thermal bremsstrahlung is the major contributor to the X-ray emission, while line cooling becomes increasingly important with lower temperatures in the post-shock region (due to less-ionized accretion species). Most IP spectra have been fit with reasonable agreement to a bremsstrahlung model plus Fe lines; however, successful fits to wide-band, high quality X-ray spectra of IPs require more sophisticated models, including multitemperature plasma models such as MKCFLOW, complex absorbers, and reflection

Table 1
Multiwavelength Observations of Swift J183920.1-045350 Enumerated in Chronological Order

Obs.	ID	Telescope	Instrument/Mode	Start Time [UT] [dd Mmm yyyy hh:mm]	Duration [ks]
1.	00044416001	Swift	XRT/PC + UVOT	21 Mar. 2013 06:59	0.5
2.	00087393001	Swift	XRT/PC + UVOT	13 Jul. 2017 06:02	3.8
3.	00087393002	Swift	XRT/PC + UVOT	14 Nov. 2017 02:42	1.1
4.	00010900001	Swift	XRT/PC + UVOT	01 Oct. 2018 17:09	1.0
5.	0821860201	XMM	PN + MOS + OM	18 Oct. 2018 11:27	26.0
6.	30360002002	NuSTAR	FPMA/B	02 Nov. 2018 08:04	40.8
7.	00088814001	Swift	XRT/PC + UVOT	02 Nov. 2018 12:30	1.4
8.	00088814002	Swift	XRT/WT + UVOT	08 Nov. 2018 13:34	0.6
9.	20335	Chandra	ACIS-I	09 Nov. 2018 08:49	2.5
10.	00087393003	Swift	XRT/PC + UVOT	07 Jul. 2019 21:29	0.2
11.	–	SALT	RSS PG900	22 Jul. 2019 19:23	1.8
12.	–	SAAO 1 m	SHOC, Clear	9 Oct. 2019	7.3
13.	–	SAAO 1 m	SHOC, Clear	13 Oct. 2019	7.2
14.	19B-340	VLA	X-band, D config.	31 Dec. 2019 19:16	7.3
15.	19B-340	VLA	X-band, D config.	03 Jan. 2020 19:14	7.3
16.	19B-340	VLA	X-band, D config.	04 Jan. 2020 19:28	7.2
17.	–	ZTF	*r*-band and g-band	continuous	–
18.	–	SAAO 1 m	SHOC, Clear	22 May 2020 23:16	15.3
19.	–	SAAO 1 m	SHOC, Clear	15 Jul. 2020 20:14	6.1
20.	–	SAAO 1.9 m	HIPPO, Clear	16 Jul. 2020 00:14	1.4
21.	–	SAAO 1 m	SHOC, Clear	16 Jul. 2020 18.31	25.3
22.	–	SAAO 1 m	SHOC, Clear	21 Jul. 2020 19:03	14.9
23.	–	SALT	RSS PG900	21 Jul. 2020 19:45	1.8
24.	–	SALT	RSS PG900	23 Jul. 2020 19:17	1.8
25.	–	SALT	RSS PG900	24 Jul. 2020 18:58	1.8
26.	–	SALT	RSS PG1800	13 Aug. 2020 21:18	0.5 × 6
27.	–	SAAO 1 m	SHOC, Clear	19 Aug. 2020	12.0
28.	–	SAAO 1 m	SHOC, Clear	22 Aug. 2020	14.6
29.	–	SALT	RSS PG1800	22 Aug. 2020 20:33	0.5 × 6
30.	–	SALT	RSS PG1800	19 Sep. 2020 18:54	0.5 × 6

(see, e.g., Lopes de Oliveira & Mukai 2019 and references therein). In a few so-called "soft" IPs, there is also a soft X-ray component (prevalent in polars) characterized by a blackbody with $T_{bb} \lesssim 100$ eV.

Nonmagnetic CVs are most often discovered in the optical, via their variability or their spectral features. Even though the number of known nonmagnetic CVs is increasing rapidly, thanks to the Sloan Digital Sky Survey (SDSS) and to recent time-domain surveys, such as the All-Sky Automated Survey for Supernovae (ASAS-SN), our census is still only complete within the immediate solar neighborhood. For example, Pala et al. (2020) constructed a volume-limited sample of CVs out to 150 pc, which includes SDSS, ASAS-SN, and Gaia discoveries, as well as one object discovered by an amateur astronomer. Magnetic CVs are, in general, the most X-ray luminous subclass of CVs, and a large majority are discovered as X-ray sources. Polars generally are soft X-ray bright sources, so the current list of polars is dominated by ROSAT-discovered objects (see, e.g., Beuermann et al. 2021 and references therein). In contrast, most IPs are hard X-ray bright and soft X-ray faint (the latter being due to strong internal absorption). As a consequence a large majority of IPs identified since 2000 have been identified in the Swift BAT and INTEGRAL hard X-ray surveys (de Martino et al. 2020). Each new X-ray survey has added to our census and understanding of magnetic CVs.

Here we present the discovery with the Niel Gehrels Swift Observatory Deep Galactic Plane Survey (DGPS; PI C. Kouveliotou) of Swift J183920.1-045350 (hereafter J1839); we also present our results of follow-up observations obtained with a multiwavelength campaign. J1839 is the second source we followed up in-depth within the scope of DGPS (Gorgone & Kouveliotou 2017). The DGPS is a Swift legacy program that covers the inner regions of the Milky Way (Phase I: $30^\circ > |\ell| > 10^\circ$ and $|b| < 0.^\circ5$). In Section 2, we outline the methods used to extract and calibrate multiwavelength data. In Section 3, we report on our subarcsecond localization, X-ray and IR spectroscopy, multiwavelength photometry, and timing analysis results. In Section 4, we discuss our IP classification of the source. Finally, a summary of our work is presented in Section 5.

2. Observations

J1839 was discovered on 2017 July 13 with the Swift DGPS with a 3.8 ks exposure, which revealed a 5.4σ detection above background (0.3–10 keV). Since this was a previously uncataloged source, we initiated a series of multiwavelength observations to identify the optical counterpart and determine the source nature. All observations are tabulated chronologically in Table 1, and described per wavelength range in detail below.

2.1. X-Ray Observations

Swift/XRT. We determined the XRT count rates, both for the DGPS discovery and for the archival XRT observation (taken on 2013 March), using the XIMAGE routine `sosta`. The DGPS count rates were multiplied by a factor (calculated using the `xrtmkarf` command) to recover the full 100% of the

enclosed-energy fraction, resulting in $1.5(3) \times 10^{-2}$ counts s^{-1} in photon counting (PC) mode. However, the source was not detected above 3σ in the single XRT archival observation of the field in 2013 March.

Chandra. We observed J1839 with Chandra ACIS-I for 2.5 ks on 2018 November 9, using one of our approved Targets of Opportunity. We analyzed the data using `fluximage` and `dmcopy` from the `ciao v4.9` package and determined the source location with subarcsecond accuracy (see Section 3.1).

XMM-Newton. We observed J1839 for 26 ks on 2018 October 18 with the XMM-Newton EPIC cameras (PN; MOS1/2) in full frame imaging mode, using one of our approved targets of opportunity. To extract the data, we used the Science Analysis Software `SAS v.1.2` and produced the final event files with `epchain` and `emchain` commands. We extracted circular source regions that contained 80% of the enclosed energy, with radii of 35″ and 25″ for the PN and MOS cameras, respectively.[21] We then extracted background regions of the same size from nearby, source-free regions. We filtered out times of high background in the 10–12 keV band and only included event patterns 0–4 for PN and 0–12 for both MOS light curves. We filtered our events file in three bands, namely 0.3–3.0 keV, 3.0–10.0 keV, and 0.3–10.0 keV, for our timing and spectral analyses. Finally, we corrected the event times to the solar system barycenter using `barycen` and the source R.A. and decl. from our Chandra observation.

NuSTAR. We observed J1839 with NuSTAR for 40.8 ks on 2018, November 2 and used the `heasoft v.6.23` command `nuproducts` to produce level 3 data. We used the same circular source region (with a radius of 120″) centered on the Chandra location, in both focal plane modules. For the background, we used a circular region of the same radius from a source-free field. We barycenter-corrected the photon arrival times to the solar system based on the Chandra position. We truncated the NuSTAR data at 20 keV, where the background started to dominate the source flux.

2.2. UV Observations

XMM-Newton/Optical Monitor. We observed J1839 with the UVM2 ($\lambda_{\rm eff} = 231$ nm), UVW1 ($\lambda_{\rm eff} = 291$ nm), and U ($\lambda_{\rm eff} = 344$ nm) filters. We used the `SAS` command `omichain` to process the data, which aggregated a final list of uniquely detected sources for each filter and produced photometric measurements for each source.

Swift/Ultraviolet-Optical Telescope. The Swift/UVOT is identical to the XMM-Newton/OM,[22] with slightly different filter throughput. We observed J1839 with the UVM2 ($\lambda_{\rm eff} =$ 225 nm), UVW1 ($\lambda_{\rm eff} = 268$ nm), and U ($\lambda_{\rm eff} =$352 nm) filters. To process these data, we used the level 3 stacked sky images produced by the HEASARC and used the HEASOFT command `uvotsource` with a 3″ radius region, centered on the Chandra location. A nearby source-free region of radius 16″ was extracted as a background reference.

2.3. Optical Observations

Zwicky Transient Facility photometry. We retrieved publicly available photometry of J1839 from the Zwicky Transient Facility Data Release 4.[23] ZTF observed J1839 sporadically between 2018 March 28 and 2020 June 28, a total of 135 times with the ZTF *g*-band filter and 241 times with the *r*-band filter. PSF photometry was automatically extracted using the pipeline in Masci et al. (2019). We found one source in ZTF data within the Chandra error circle.

Southern African Large Telescope (SALT) spectroscopy. Spectroscopy of J1839 was undertaken with SALT (Buckley et al. 2006) during one night in 2019 and six in 2020 (see Table 1). The Robert Stobie Spectrograph (RSS; Burgh et al. 2003) was used, initially with the PG900 VPH grating, covering the region 4060–7120 Å at a mean resolution of 4.7 Å with a 1.″5 slit width. All exposures were 1800 s. The last three observations utilized the PG1800 VPH grating, covering 5800–7100 Å at a resolution of 2.4 Å, also with a 1.″5 slit. Six 500 s exposures were taken. For all observations, wavelength calibration lamp exposures were taken immediately following the observations on each night.

The spectra were reduced using the PySALT package (Crawford et al. 2010),[24] which does bias, gain, and amplifier cross-talk corrections, mosaics the three CCDs and applies cosmetic corrections. Object extraction, wavelength calibration and background subtraction were all done using standard IRAF[25] routines, as was the relative flux calibration.

South African Astronomical Observatory (SAAO) photometry and photopolarimetry. Time series photometry of J1839 was undertaken on eight nights (see Table 1) using the SAAO 1 m telescope[26] with the Sutherland High speed Optical Camera (SHOC) CCD camera. SHOC uses an Andor iXon888 frame transfer EM-CCD camera, with 1024×1024 pixels (Coppejans et al. 2013). All observations were done in conventional (non-electron-multiplying; EM) mode without a filter (i.e., "white light"); an exposure time of 30 s was used.

Reduction of the CCD images included subtraction of median bias and flat-field correction using median-combined frames from exposures of the twilight sky. Aperture-corrected photometry was used to extract the light curves of all stars in the calibrated science images and differential photometry was performed using several local reference stars.

Time resolved filterless all-Stokes polarimetry of J1839 was obtained on 2020 July 15, over a period of ∼1400 s with the HIPPO photopolarimeter (Potter et al. 2010).

2.4. Radio Observations

Karl G. Jansky Very Large Array (VLA). We were allocated 6 hr of Director's Discretionary Time (DDT) to observe J1839 with the Karl G. Jansky Very Large Array (VLA) in the X-band (8–12 GHz). X-band was chosen to maximize sensitivity, while decreasing Radio Frequency Interference (RFI). Despite the band selection, both observations were significantly affected by RFI, and we removed bands above 10.8 GHz to mitigate spurious signals. All VLA observations used the 3 bit continuum mode with 4 GHz of continuous bandwidth. In our first observation (Obs. 15 in Table 1), J1839 was observed with 27 antennas. In Obs. 16 and 17, 19, and 25 antennas were used, respectively. Throughout all of our observations, we used

[21] See Section 3.2.1.1 of the XMM Users Handbook: https://heasarc.gsfc.nasa.gov/docs/xmm/uhb/onaxisxraypsf.html.

[22] Swift/UVOT modules are the flight spares of the XMM-Newton/OM, see https://swift.gsfc.nasa.gov/about_swift/uvot_desc.html.

[23] https://www.ztf.caltech.edu/page/dr4

[24] https://astronomers.salt.ac.za/software/pysalt-documentation/

[25] https://iraf.noao.edu/

[26] See https://www.saao.ac.za/astronomers/telescopes-1-0m/ for telescope details.

Table 2
Fundamental Properties of J1839

Parameter	Value	Citation
$\text{Luminosity}_{0.4-20\ \text{keV}}$	$2.71^{+2.69}_{-0.91} \times 10^{33}$ erg s^{-1}	This work
P_s	449.7 s	This work
P_o	5.6 ± 0.3 hr	This work
Distance	$2.3^{+1.9}_{-0.8}$ kpc	Bailer-Jones et al. (2018)
μ_α	-1.1 ± 0.4 mas yr^{-1}	Gaia Collaboration et al. (2018)
μ_δ	-2.6 ± 0.4 mas yr^{-1}	Gaia Collaboration et al. (2018)

J1832-1035 as the complex gain calibrator. We used 3C48 (J0137+3309) as the flux density and bandpass calibrator. We note that 3C48 was known to undergo flaring activity at the time of the observation, causing the absolute flux density estimates to be uncertain to ∼10%.

3. Results

Here we describe the source localization, and the temporal and spectral analysis results. A comprehensive summary of source characteristics can be found at Table 2.

3.1. Localization, Distance, and Proper Motion

We determined the Chandra location of J1839 using `wavdetect` with `ciao v4.9` (Obs. 9 in Table 1). We found one source at R.A. $18^h39^m19^s.98$, decl. $-04°\ 53'\ 53''.1$ (J2000) with a positional uncertainty of $0''.8$ (90% confidence, systematic error) within the astrometrically corrected XRT-UVOT position (ACP). The latter was calculated using the method described in Evans et al. (2014). Figure 1 shows the Chandra field with the XRT/ACP error circle (green) superposed on the Chandra source (red). The XRT/ACP location center is offset from the Chandra location by $0''.683$.

Further, we searched the Gaia DR2 data Gaia Collaboration et al. (2018) within the Chandra uncertainty region. We identified one source, Gaia DR2 4256603449854150016 ($G_{\text{Gaia}} = 18.5$), which is offset from the Chandra location centroid by $0''.193$ (black cross, Figure 1). Taking into account the significantly larger Swift/XRT point-spread function, we conclude that the Chandra and Gaia sources are indeed the counterparts of J1839.

Finally, we adopt the distance and proper motion of the Gaia source for J1839 for the remaining analysis. The former is estimated to be $2.26^{+1.93}_{-0.83}$ kpc (68% confidence; Bailer-Jones et al. 2018). The proper motion is $\mu_\alpha,\ \mu_\delta = -1.1 \pm 0.4, -2.6 \pm 0.4$ mas yr^{-1}, where the uncertainties are expressed as standard errors by the Gaia Collaboration et al. (2018). In Section 3.3, we discuss the optical and IR photometry results within the source distance context.

3.2. Spectroscopy

We observed J1839 in three different wavebands: in the X-rays (0.5–20 keV), and in the optical between 4000–7000 Å and 5500–9000 Å. Below we describe our spectral analyses.

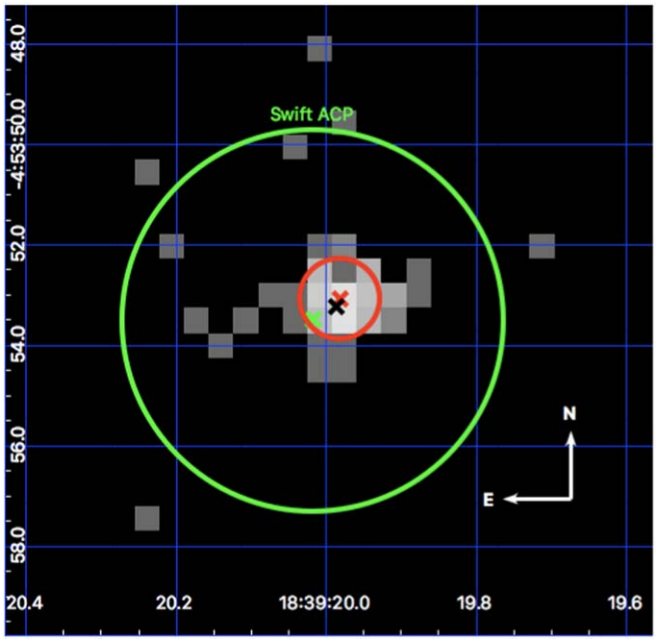

Figure 1. Chandra image (Obs. 9 from Table 1) with the `wavdetect` position and pointing uncertainty ($\sim 0''.8$) in red, the XRT/ACP position with a 90% uncertainty circle from Obs. 2 (green), and the Gaia location (black x, uncertainty of ∼0.2 mas). The image is binned at the native plate scale of Chandra, 1 pixel $\sim 0''.5$.

3.2.1. X-Ray Spectrum

We used the NuSTAR and XMM-Newton data for our spectral fits, as these were the highest quality data sets. We first visually inspected the data, and found a deviation from a smooth spectrum in the 6–7 keV range. This was most significant in the PN spectrum (Figure 2).

The XMM-Newton and NuSTAR spectra were first fitted separately with XSPEC with an absorbed power law (PL) to identify general broadband spectral properties. A constant prefactor was used to allow for simultaneous fitting across all EPIC cameras (XMM-Newton) or Focal Plane Modules (NuSTAR; FPMA and FPMB). The prefactor was set to 1 in the first spectrum in the group, and all others were left free to vary. To check for spectral evolution, we first fit both data sets with a PL in their overlapping spectral range (3–10 keV); these fits yielded PL indices of $\Gamma = 1.3^{+0.3}_{-0.2}$ in the XMM-Newton data (1σ uncertainties) and $\Gamma = 2.2 \pm 0.2$ in the NuSTAR data (1σ uncertainties). Therefore, J1839 appeared to have varied significantly over the ∼ 15 day period between observations 5 and 6 in Table 1. However, large positive residuals remained in the 6–7 keV range, which encompasses the Fe line complex (top middle panel of Figure 3), so we added a Gaussian component to account for the Fe lines. We refer to this absorbed PL plus Gaussian as Model 1. This model provided a good fit to both individual spectra with a reduced $\chi^2 = 167.33/208 = 0.84$ for XMM-Newton and $\chi^2 = 171.78/191 = 0.93$ for the NuSTAR spectrum. All best-fit parameter values agreed within 1σ in both instruments, therefore, we proceeded in fitting the two data sets together.

We also used a prefactor for each spectrum in the joint fits with Model 1. The prefactors varied less than 10% for all XMM-Newton instruments; we chose to freeze the PN factor to 1. For NuSTAR, the prefactors were best fit at 1.43 and 1.23 for FPMA and FPMB, respectively; the prefactor for FPMA

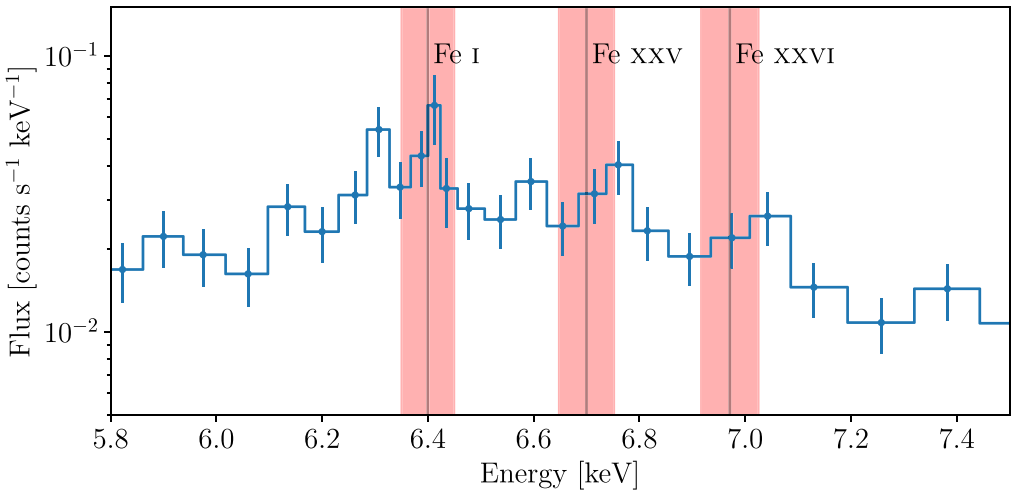

Figure 2. Fe spectral lines as observed with XMM-Newton EPIC PN are shown together with their rest energies (red shaded regions). The possible energy shifts in the lines correspond to a source velocity along the line of sight of $|v_r| \leqslant 2.34 \times 10^3$ km s^{-1}.

is $\geqslant 16\%$ greater than FPMB for all models tested. This discrepancy could be due to a rip in the multilayer insulation recently reported by Madsen et al. (2020).

Motivated by the optical spectra that suggested that J1839 was a CV (see below), and quite possibly an IP, we introduced Model 2. Model 2 comprises two absorbing columns (tbabs for interstellar medium and pwab—Done & Magdziarz 1998—for a local partial covering absorber) with a broadband, isobaric cooling flow component (`mkcflow`) and a Gaussian for the ∼6.4 keV spectral line. While fitting Model 2, the nHmin parameter of pwab was frozen to 1.0×10^{15} cm^{-2} and the lowT parameter was frozen to 0.0808 keV. The redshift parameter of `mkcflow` was set to the minimum 1.0×10^{-7}, given the Gaia source distance of ∼2 kpc. We show the best-fit result in the top panel of Figure 3. Similar prefactor values were found for both Models 1 and 2.

Finally, we fit the data with an absorbed PL with three Gaussians (referred to as Model 3), corresponding to the ionized Fe lines typically seen in CVs (Hellier et al. 1998; Ezuka & Ishida 1999; Hellier & Mukai 2004), and also suggested by the PN spectrum (Figure 2). These narrow line components were frozen at central energies of 6.4, 6.7, and 6.97 keV and their standard deviations were frozen at 0.0 keV (one spectral bin width). This model is highlighted in the bottom panel of Figure 3 (top subpanel), with associated residuals shown in the lower subpanel. We compare all three models in Section 4.

To obtain the source fluxes with each of these models, we froze the model normalizations and added a `cflux` component to the spectral model to measure unabsorbed flux. We set the energy band from 0.3 to 20.0 keV. The resulting values are reported in the last row for each model in Table 3. For spectral Model 2, we calculate a luminosity of $L_{0.3-20.0} = (2.44^{+2.43}_{-0.85}) \times 10^{33}$ erg s^{-1}, based on the unabsorbed flux and the Gaia counterpart distance. The flux and distance fractional uncertainties were added in quadrature; the distance uncertainty contributed to the large upper uncertainty of the luminosity.

3.2.2. Optical Spectra

Figure 4 shows the averaged flux-calibrated SALT RSS spectrum of J1839, where we combined the two highest signal-to-noise spectra obtained on 2020 July 21 and 23, respectively. The spectrum is characterized by strong H I (Balmer), He I, and He II emission lines, on top of a continuum that rises to the red. This spectrum establishes J1839 as a likely CV. The Hα emission is the strongest and we also see both the high excitation He II 4686 Å and Bowen fluoresence (4640–4660 Å) lines, both a common feature seen in magnetic CVs as a result of the ionizing soft X-ray emission (McClintock et al. 1975; Mukai 2017). Whereas the He II 4686 Å line can be brighter than the neighboring Hβ line in polars, it is typically weaker in IPs.

Given the strength of the Hα line, we obtained higher resolution SALT spectra (using the PG1800 grating on RSS) on three different nights in 2020 August–September (Obs. 26, 29, and 30 in Table 1). The inserts in Figure 4 show the varying Hα profiles. From night to night there is clear variability in the line profile but unfortunately the coverage of the high resolution spectra is too sparse to look for coherent variability on the timescale of a possible orbital period.

3.3. Photometry

We searched with the VOSA tool (Bayo et al. 2008) for archival data within 2″ of the Chandra position of J1839. We found a candidate counterpart in the Panoramic Survey Telescope and Rapid Response System (Pan-STARRS, Chambers et al. 2016) *g*, *r*, *i*, *z*, and *y* bands, PSO J183919.988 −045353.099 (PS1 identifier 102122798332882651), which is 0.″178 offset from J1839. We then searched the Gaia data release 2 (Gaia Collaboration et al. 2018) and found G, G_{BP}, and G_{RP} magnitudes of the source Gaia DR2 4256603449854150016, which is offset by 0.″193 from the Chandra position of J1839 (see also Figure 1).

3.3.1. SAAO High Speed Optical Photometry

Figure 5 shows the SAAO high speed photometry of J1839 for five of the longest observing runs in 2020. The data were obtained in white light (unfiltered) and calibrated using Pan-STARRS *r*-band photometry of reference stars in the field. Such a calibration is only accurate to ∼0.1 mag, see the discussion in Coppejans et al. (2014). J1839 is around

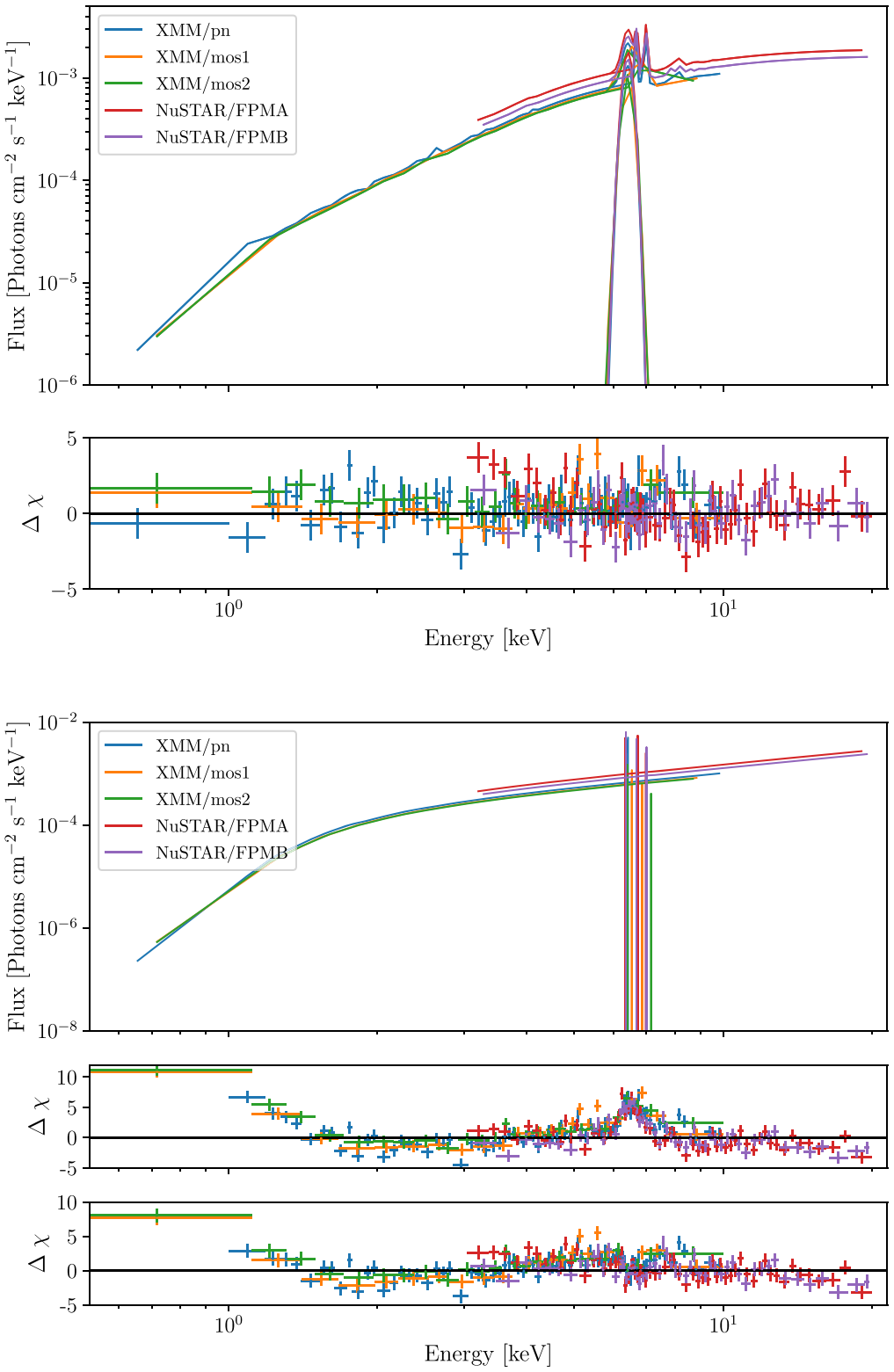

Figure 3. XMM-Newton and NuSTAR spectral models are shown in the upper panels with the data residuals in the lower panels. (Top) Spectral Model 2 fit. (Bottom) Spectral Model 3 fit with associated residuals (top and bottom subpanels) as described in Table 3; the middle subpanel shows residuals of the `constant*tbabs (powerlaw)` fit. Data are binned to a minimum significance of 5σ for visual clarity.

18.4 mag during these observations. In Figure 5, Obs. 18 is shown at the correct brightness and subsequent runs have been offset for display purposes. The light curves show the characteristic variability of a CV. In parts of the light curve, the sideband optical modulation at 459.89 s (see the next session), is visible by eye, e.g., in the first half of the light curve of Obs. 28. No clear orbital modulation on timescales of ∼5 hr is visible in the light curves.

Table 3
Best-fit Parameters for Models 1, 2, and 3

Model	Parameter	Value ±90% Confidence	Unit
bf1. PL + Gaussian	TBabs: $N_{\rm H}$	$1.58^{+0.31}_{-0.25}$	10^{22} cm^{-2}
Cstat = 2308	PhoIndex	$1.02^{+0.07}_{-0.07}$	
2812 d.o.f	PL norm	$1.06^{+0.17}_{-0.14}$	10^{-4}
or	LineE	$6.50^{+0.05}_{-0.07}$	keV
$\chi^2 = 2518.91$	Gaussian Sigma	$0.45^{+0.16}_{-0.09}$	keV
2812 d.o.f.	Gaussian: norm	$2.94^{+0.55}_{-0.41}$	10^{-5}
$\chi^2_{\rm red} = 0.90$	unab. Flux$_{0.3-20.0}$	$2.87^{+0.16}_{-0.15}$	10^{-12} erg s^{-1} cm^{-2}
2. mkcflow + Gaussian	Tbabs: $N_{\rm H}$	$0.33^{+0.18}_{-0.16}$	10^{22} cm^{-2}
Cstat = 2144	pwab: nHmax	$29.05^{+21.07}_{-9.12}$	10^{22} cm^{-2}
2809 d.o.f.	pwab: beta	$-0.38^{+0.08}_{-0.07}$	
or	mkcflow: highT	$63.18^{+16.72]}_{-26.52}$	keV
$\chi^2 = 2350$	mkcflow: Abundanc	$1.69^{+1.07}_{-0.90}$	
2809 d.o.f.	mkcflow: norm	$8.85^{+8.39}_{-2.58}$	10^{-12}
$\chi^2_{\rm red} = 0.84$	Gaussian: LineE	$6.41^{+0.08}_{-0.05}$	keV
	Gaussian: Sigma	$13.83^{+9.78}_{-8.03}$	10^{-2} keV
	Gaussian: norm	$1.23^{+0.44}_{-0.29}$	10^{-5}
	unab. Flux$_{0.3-20.0}$	$4.31^{+0.47}_{-0.39}$	10^{-12} erg s^{-1} cm^{-2}
3. PL + 3 Gaussians	TBabs: $N_{\rm H}$	$1.89^{+0.31}_{-0.27}$	10^{22} cm^{-2}
Cstat = 2335	powerlaw: PhoIndex	$1.08^{+0.07}_{-0.07}$	
2812 d.o.f	powerlaw: norm	$1.25^{+0.18}_{-0.15}$	10^{-4}
	Gaussian: LineE	6.40	keV
or	Gaussian: Sigma	0.0	keV
	Gaussian: norm	$1.02^{+0.15}_{-0.14}$	10^{-5}
$\chi^2 = 2537$	Gaussian: LineE	6.70	keV
2812 d.o.f.	Gaussian: Sigma	0.0	keV
$\chi^2_{\rm red} = 0.90$	Gaussian: norm	$6.75^{+1.48}_{-1.40}$	10^{-6}
	Gaussian: LineE	6.97	keV
	Gaussian: Sigma	0.0	keV
	Gaussian: norm	$4.30^{+1.26}_{-1.20}$	10^{-6}
	unab. Flux$_{0.3-20.0}$	$2.94^{+0.16}_{-0.16}$	10^{-12} erg s^{-1} cm^{-2}

Note. Model 1: `constant*tbabs(powerlaw+Gaussian)`. Model 2: `constant*phabs*pwab(mkcflow + Gaussian)`. Model 3: `constant*Tbabs(powerlaw + Gaussian + Gaussian + Gaussian)`. Brackets on parameters denote that the uncertainty extends to the upper (⌉) or lower limit (⌊) of the model parameter allowed by XSPEC.

3.3.2. Optical Polarization

The HIPPO photopolarimetry measurements of J1839 did not detect circular polarization, typical of magnetic CVs, particularly polars ($\langle V/I\rangle = 0.01\%$ S.D. $= 0.46\%$). Since most IPs do not show detectable polarization, this is not surprising. The mean linear polarization value was $\langle p\rangle = 1.47\%$ with S.D. $= 0.67\%$, with no obvious variability. This is consistent with an interstellar origin. The position angle of the linear polarization is $\theta = 95^\circ \pm 12^\circ$, also consistent with an ISM origin.

3.3.3. UV and Optical

For the Swift/UVOT we used the command `uvotsource` in the `heasoft v6.23` to determine the source AB magnitude (uncorrected for extinction); these are reported in column 6 of Table 4.

In the XMM-Newton/OM, we used the SAS routine `omdetect` (method 1) to find counterparts in the U and UVW1 filters, which were detected at 26.89σ and 8.11σ significance, respectively. These candidate counterparts are $1\farcs10$ and $1\farcs29$ from the Chandra location, respectively. Both sources have nonzero quality and confusion flags, which we address below. The latter is expected in crowded regions like the Galactic plane.

The UVW1-band source is within an area of enhanced emission (possibly diffuse) and has a bad pixel (QFLAG = 33). There were also one or more sources detected at a distance of 6–12 pixels (CFLAG = 1). Source confusion was checked visually, and the `omdetect` region centroid is centered on the source without significant light from neighboring sources.

The *U*-band source has the same flags as the UVW1-band; however, it also lies near a bright source (total QFLAG = 97) and has one or more sources 3–6 pixels away (total CFLAG = 3). The former flag is quite possibly due to the increased sensitivity and spectral breadth compared to the UVW1-band as well as the source lying within the Galactic plane.[27] Similarly, the source region was visually inspected and deemed acceptable with little neighbor contamination.

[27] See https://xmm-tools.cosmos.esa.int/external/xmm_user_support/documentation/uhb/omfilters.html.

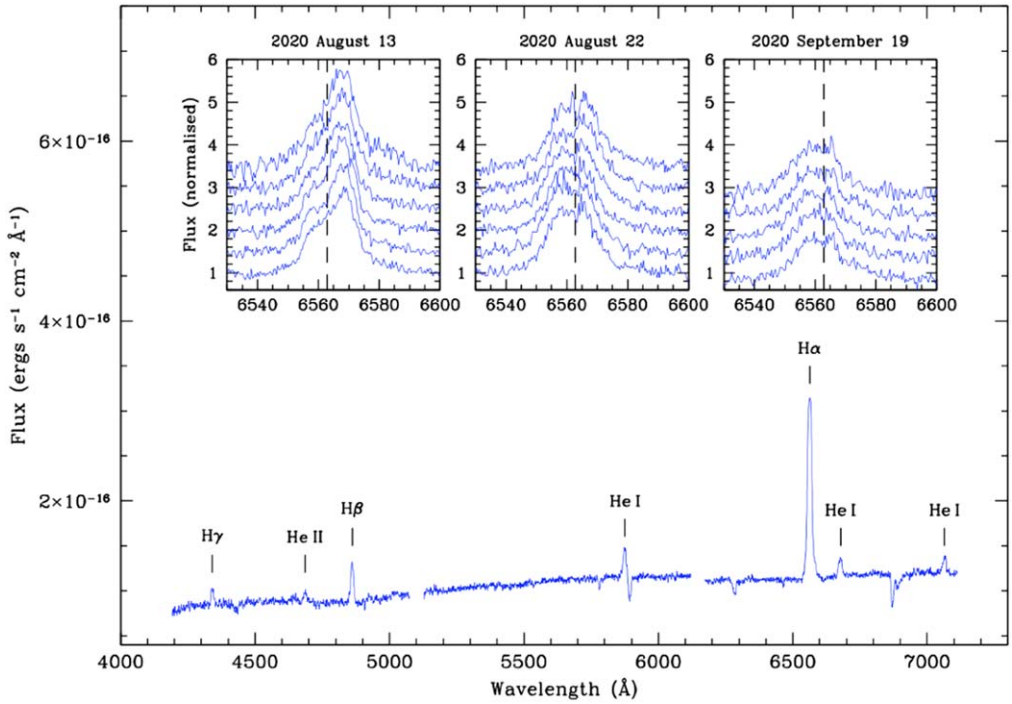

Figure 4. The average SALT RSS spectrum of J1839 covering the wavelength range of 4190–7100 Å. The main emission lines are marked and labeled. The insets show the varying Hα emission line profiles as observed at higher spectral resolution (PG1800) on SALT on three different days; each sequence shows a series of consecutive 500 s spectra (first to last: bottom to top). The vertical dashed line in the insets indicates the rest wavelength of Hα.

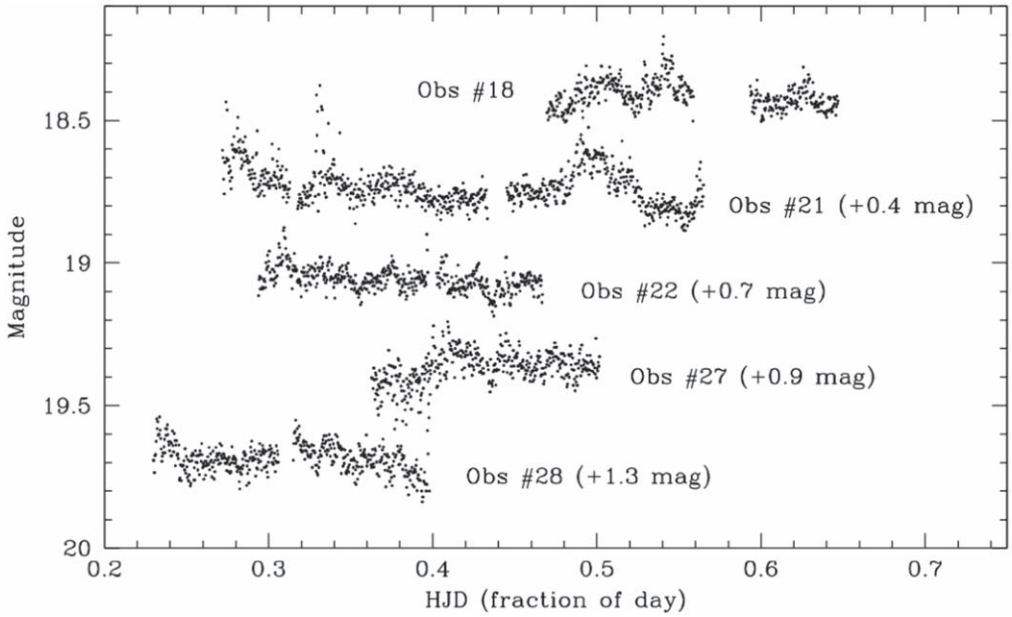

Figure 5. Light curves of J1839 taken with SAAO 1 m telescope. Obs. 18 is shown at the correct brightness, whereas subsequent observing runs have been displaced vertically for display purposes only. The data are calibrated to the Pan-STARRS *r* band.

3.3.4. Radio

We find no radio sources at or near the Chandra position. The closest source, an unidentified radio triple, is $\sim 30''$ away. The 3σ upper limits (i.e., $3\times$ rms noise) at the Chandra position are 43μ Jy at 9.75 GHz for Obs. 14; 38μ Jy at 9.75 GHz for Obs. 15; and 28μ Jy at 9.37 GHz for Obs. 16. We combined the data from Obs. 14–16 and obtained a 3σ upper limit of 22μ Jy at an effective central frequency of 9.37 GHz with a 2.75 GHz bandwidth.

3.4. Timing

We searched the XMM-Newton, NuSTAR, and SAAO data for periodicities. For XMM-Newton we created a Z_1^2 statistic (Buccheri et al. 1983), in the 0.3–10.0 keV band of EPIC PN. The resulting power spectrum showed a maximum at $(2.228 \pm 0.004) \times 10^{-3}$ Hz, i.e., a period of 448.7 ± 0.3 s. We also generated Lomb–Scargle periodograms using data collected with EPIC PN, MOS1, and MOS2 in the same energy band. We find a significant peak at 448.0 ± 0.7 s in the PN data consistent

Table 4
Observations of Swift J183920.1-045350 by UVOT

Obs.	ID	Telescope	Start Time (UT)	Filter	Magnitude (or 5σ Limit)
			(yyyy Mmm dd hh:mm)		(AB mag)
1.	00044416001	UVOT	2013 Mar 21 06:59	UVM2	>21.22
2.	00087393001	UVOT	2017 Jul 13 06:02	UVW1	†
3.	00087393002	UVOT	2017 Nov 14 02:42	UVW1	†
4.	00010900001	UVOT	2018 Oct 01 17:09	U	$19.70 \pm 0.15 \pm 0.02$
5.	0821860201	OM	2018 Oct 18 11:27	UVW1	19.67 ± 0.05
				U	18.43 ± 0.02
7.	00088814001	UVOT	2018 Nov 02 12:30	U	$20.28 \pm 0.10 \pm 0.02$
8.	00088814002	UVOT	2018 Nov 08 13:34	UVM2	>21.11
10.	00087393003	UVOT	2019 Jul 07 21:29	UVW1	†

Note. Swift magnitude uncertainties shown are statistical first (when available) then systematic uncertainties. †: Source projected out of the field of view. Obs. column corresponds to the observation in Table 1.

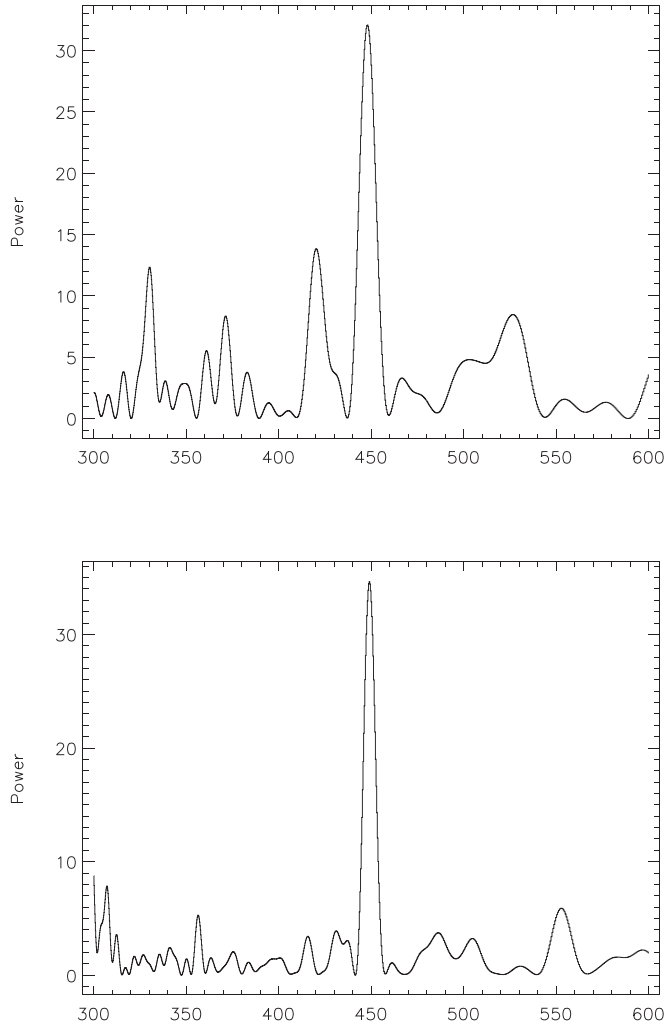

Figure 6. Lomb–Scargle periodogram using the full energy range of XMM-Newton. (Top) EPIC PN data. (Bottom) MOS2 data.

with the Z^2 results (see the top panel of Figure 6). The signal is also highly prominent and consistent in MOS2 (448.9 ± 0.3 s, see the bottom panel of Figure 6). The MOS1 periodogram also shows the signal at the same period but much less significant due to the fact that the source was placed near the chip gaps of the detector.

To search for periodicities in the NuSTAR data, we corrected the photon arrival times to the solar system barycenter using the HEASOFT V.6.23 command `hdaxbary`. We set the location to the source centroid measured with Chandra. We extracted source events from the 80% enclosed-energy fraction radius of 75″ for the most conservative 3−4.5 keV energy range (An et al. 2014, Figure 5). A Lomb–Scargle frequency analysis of the NuSTAR data (FPMA and B) shows a peak at $f_{\rm NuSTAR1} = (2.2268 \pm 0.0016) \times 10^{-3}$ Hz, consistent with the peak frequencies observed in the XMM observations, but with considerably better accuracy. The resulting power spectrum is shown in the lower panel of Figure 8. The X-ray period is 449.1 ± 0.3 s. A Z_1^2 test in the combined FPMA and FPMB NuSTAR data within a 3–30 keV range, found a 5σ peak at $f_{\rm NuSTAR2} = (2.2239 \pm 0.0017) \times 10^{-3}$ Hz, corresponding to an X-ray period of 449.7 ± 0.6 s. Given that the above period values are all consistent within $\sim 1\sigma$, and also taking into account the extended energy range of the latter estimate, as well as the significant jitter associated with WD timing, we adopt NuSTAR2 as the spin period of J1839, as it is far too short to be the orbital period of a nondegenerate hydrogen-rich CV. Littlefield et al. (2016) demonstrated a pronounced (almost 0.2 cycle) phase shift in the optical spin pulse of FO Aqr when it entered a low state (see their Figure 5). Unfortunately, the period determined with the XMM-Newton data is not accurate enough to phase-connect with the NuSTAR observation; Figure 7, therefore, demonstrates the relative phase shift between the two observations. While phase jitters have not been directly observed in X-rays, Hellier (1997) observed orbital phase shift in the eclipse egress timing in XY Ari, which they interpret as random shifts in the position of the accreting spots in that IP.

We then folded all three EPIC camera light curves with the 449.7 s period (Figure 7), using the `fold_events` command in Python package STINGRAY V.0.1 (Huppenkothen et al. 2019). The folded pulse profiles were fit with the first harmonic function of Bildsten et al. (1997), i.e., $\mathrm{A}\sin(2\pi\phi) + \mathrm{B}\cos(2\pi\phi) + \mathrm{C}$, with parameters A, B, and C free to vary. The resulting best-fit parameters, their standard deviations (σ_X), and χ^2 fit statistic are reported in Table 5.

We calculated the rms pulsed fraction ($\mathrm{PF_{rms}}$) using Equation (1).

$$\mathrm{PF_{RMS}} = \mathrm{C}^{-1}\sqrt{0.5 \times (\mathrm{A}^2 + \mathrm{B}^2 - \sigma_{\mathrm{A}}^2 - \sigma_{\mathrm{B}}^2)}. \quad (1)$$

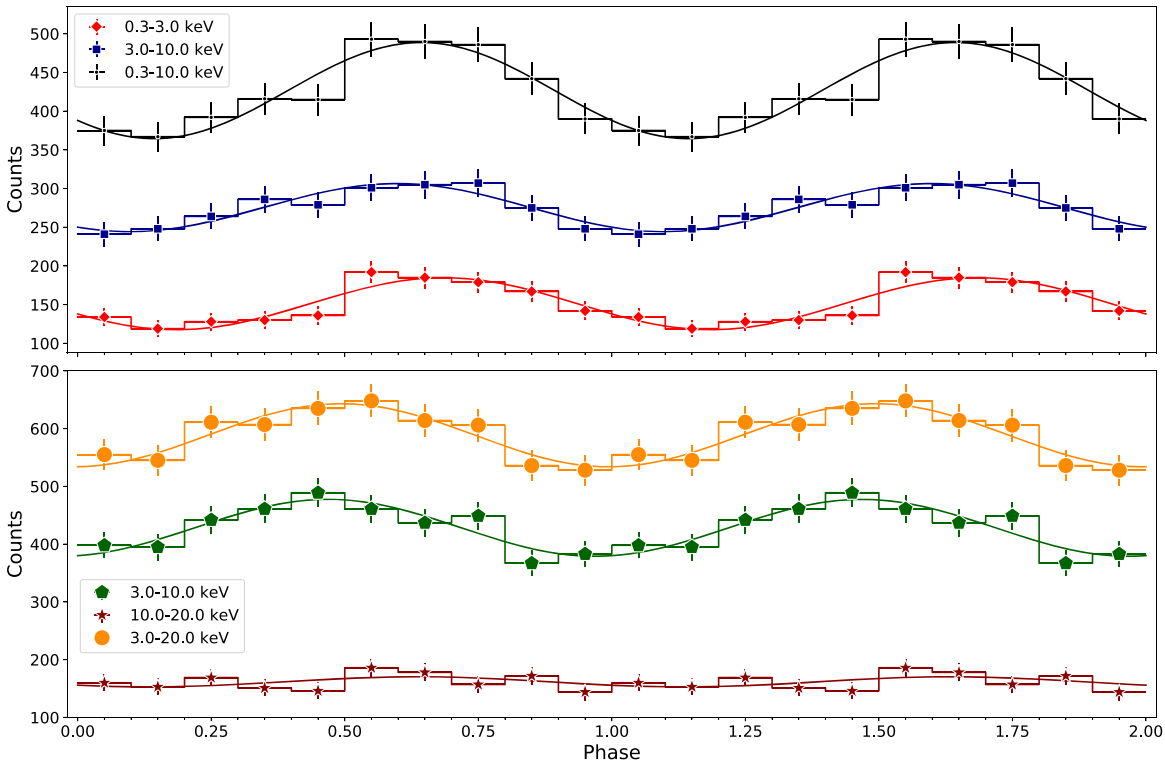

Figure 7. Pulse profile using (top) the combined XMM-Newton EPIC cameras in three energy bands from Obs. 5 and (bottom) the combined focal plane modules of NuSTAR in three energy bands. The data plotted are repeated over two full periods for visual clarity, in bins of 0.1 period, i.e., ∼44.97 s.

Table 5
Best-fit Parameters for the Pulse Profile Model C+Asin(2πϕ)+Bcos (2πϕ) Are Shown for Energy Bands from Observations 5 and 6

Parameter (Units)	Combined XMM EPICs			Combined NuSTAR FPMs		
	0.3–3.0 keV	3.0–10.0 keV	0.3–10.0 keV	3.0–10.0 keV	10.0–20.0 keV	3.0–20 keV
Constant, C (cts)	151.20 ± 3.45	275.40 ± 3.11	426.60 ± 5.22	428.20 ± 5.73	161.60 ± 4.49	588.50 ± 5.43
Amplitude A (cts)	−30.82 ± 4.87	−17.84 ± 4.40	−48.66 ± 7.38	9.67 ± 8.11	−6.53 ± 6.35	2.19 ± 7.68
Amplitude B (cts)	−13.30 ± 4.87	−25.30 ± 4.40	−38.60 ± 7.38	−48.13 ± 8.11	−5.80 ± 6.35	−54.50 ± 7.68
Pulsed Fraction (%)	15.0 ± 3.0	7.6 ± 2.3	10.0 ± 1.7	7.9 ± 2.4	[a]	6.4 ± 1.9
χ^2 ($\chi^2_{\rm RED}$; 7 DOF)	5.37 (0.77)	2.42 (0.35)	4.53 (0.65)	4.24 (0.61)	6.63 (0.95)	2.76 (0.39)

Notes. Errors are at the 68% confidence interval.
[a] The pulsed fraction could not be determined, due to a low number of pulsed counts.

To calculate the uncertainty on PF_{rms}, we performed 10^4 simulations of the pulse profile. In each simulation we created a synthetic pulse profile by drawing data points from Gaussian distributions. The Gaussian was unique to each phase bin, with a mean equal to the bin value and standard deviation equal to the bin uncertainty. Each synthetic pulse profile was fit with the same model described above, and the pulsed fraction was recorded. After all simulations were complete, we created a histogram of PF_{rms} values, which was fit with a Gaussian. The standard deviation of the best-fit Gaussian was taken to be the uncertainty of PF_{rms}. We used the same methods as in the XMM-Newton data to plot and determine the pulsed fraction in the NuSTAR data.

The 2020 SAAO high speed photometry was used to search for coherent short-period optical modulations. We employed the generalized Lomb–Scargle period search as implemented in VARTOOLS (Hartman & Bakos 2016) to identify peak frequencies in the optical data. The top panel of Figure 8 shows the Lomb–Scargle periodogram of the SAAO photometry between 1.2 and 3.2 mHz (left side), and a zoomed in view between 2.1 and 2.3 mHz (right side). A clear peak is identified at 2.17441×10^{-3} Hz with a formal false alarm probability of 1.1×10^{-14}, which we associate with the beat frequency $(\omega - \Omega)$, where ω is the spin frequency determined from the X-ray data, and Ω is the inferred orbital frequency. The optical beat frequency corresponds to a period of 459.89 ± 0.13 s. When interpreted using the 449.7 ± 0.3 X-ray spin period, this implies that the inferred orbital period is 5.6 ± 0.6 hr, where the error is dominated by the uncertainty in the X-ray spin frequency.

After prewhitening the optical data with the beat frequency, a small residual remains at the location of the X-ray spin frequency. This is shown in the middle panels of Figure 8. The zoomed in

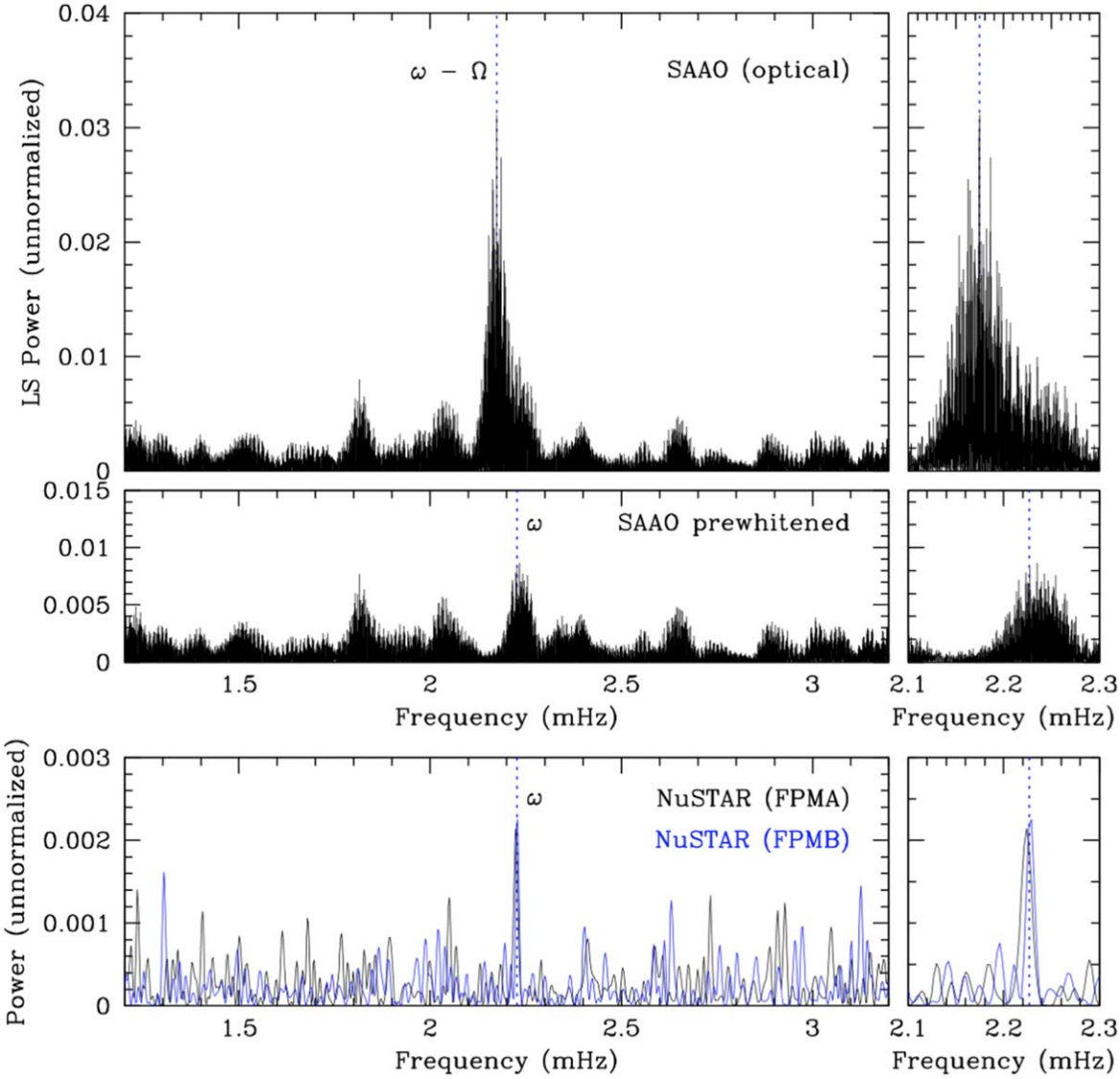

Figure 8. Lomb–Scargle periodograms of the optical data from SAAO (top and middle panels) and the X-ray data from NuSTAR (lower panels). The left panels show the periodogram over a wide frequency range (1.2–3.2 mHz), whereas the right panels zoom in on the peaks associated with the spin and the beat frequencies over a narrow frequency range (2.1–2.3 mHz). The middle panels show the residual signal after prewhitening with the dominant beat frequency ($\omega - \Omega$) identified in the top panel.

view (middle right panel) shows a number of alias peaks around the X-ray spin frequency (vertical dashed line), making it hard to improve on the exact determination of the spin frequency. Nonetheless, there is clearly some power in the optical Lomb–Scargle periodogram at the spin frequency. The simultaneous presence of spin and beat periods in the optical is typical of IPs (Warner 1986; Pretorius 2009; Littlefield et al. 2016). The relative strength of the beat modulation indicates that optical pulses are dominated by the X-rays reprocessed by structures fixed in the binary frame, such as the secondary or the bright spot where the accretion stream interacts with the accretion disk.

In general, the SAAO photometric runs are less than 5 hr in length, with only one long observing run of 7 hrs (Obs. 21). This, together with the complex alias structure in the power spectrum, dominated by the ∼5 day sampling, makes it hard to reliably identify low frequency orbital modulations in the SAAO data. However, two period maxima are seen in the power spectrum, close to the purported $\sim 5.6 \pm 0.3$ hr orbital modulation, at 5.25 and 5.49 hr. We searched for longer periods using the more extensive coverage ZTF photometry of J1839 in the *r* band and found a peak in the power spectrum at 5.448 hr, consistent with the predicted orbital period, although similar power is seen at several of the 1 cycle day^{-1} aliases on either side.

4. Discussion

The intrinsic properties of J1839 derived above and summarized in Table 2 are typical of known IPs: the X-ray luminosity is typical (Pretorius & Mukai 2014), and the measured spin period and the inferred orbital period are both well within the normal range for IPs (Mukai 2017). Further, the success of our X-ray spectral modeling shows that the X-ray emission may originate in hot plasma, possibly having a multitemperature nature, that is located next to a cold surface containing Fe of low ionization states. As to the optical magnitude and color, we must first account for interstellar reddening. The 3D extinction map of Lallement et al. (2019)[28] only extends to 2.25 kpc in this direction, and gives an

[28] Available online at https://stilism.obspm.fr/.

extinction of $E_{B-V} = 1.08 \pm 0.45$ mag at that distance. The lower end of this range may be appropriate for J1839, since the MKCFLOW fits to the X-ray spectrum suggests an interstellar N_H of $3.3^{+1.8}_{-1.6} \times 10^{21}\,\mathrm{cm}^{-2}$, or $E_{B-V} \approx 0.5$. Given these uncertainties, it is impossible to be precise, but the location of J1839 will likely fall in a location occupied by the majority of IPs as compiled by Abril et al. (2020). Thus, J1839 appears to be a typical IP seen at a larger than typical distance, thus extending the reach of the CV population in our Galaxy.

The discovery of J1839 serves as a reminder that deeper X-ray surveys of the Galactic plane will likely yield detection of an increasing number of IPs. The large majority of currently known IPs (50 out of 69 according to de Martino et al. 2020 have been detected in hard X-ray surveys using coded-mask aperture instruments (Swift/BAT and INTEGRAL). These surveys are capable of detecting IPs with luminosity of $\sim 10^{33}$ erg s^{-1} out to distances of 1–2 kpc.

The work presented here also demonstrates the importance of detecting IPs far away from the solar neighborhood in a systematic manner. While a number of even more distant IPs have been reported, those close to Galactic center distances are not suitable for detailed multiwavelength studies such as the one we have performed. Moreover, very distant IPs discovered serendipitously cannot be reliably used for statistical population studies. Future DGPS discoveries of IPs have the potential to lead to a direct observational study of the Galactic distribution of CVs, a subject rarely discussed in the literature, with a few exceptions, e.g., Britt et al. (2015). Such studies will place the estimates of the CV contributions to the Galactic ridge on much firmer ground (Mukai & Shiokawa 1993).

Deep X-ray surveys might also uncover a relatively nearby population of low luminosity IPs (LLIPs), if such objects exist (Pretorius & Mukai 2014). Current indications are that there is a deficit of IPs with X-ray luminosities in the 10^{32} to 10^{33} erg s^{-1} range, but perhaps with a separate population of LLIPs below 10^{32} erg s^{-1}. DGPS and other future X-ray surveys have the potential to confirm or refute this possibility.

5. Conclusions

We described the multiwavelength follow-up of the source J1839, discovered within the scope of the DGPS. We found source counterparts in Gaia and Pan-STARRS data, which allowed us to determine source location, distance, and proper motion. We detected counterparts to J1839 in the UV, optical, and IR regimes; however, no counterpart was found in the radio *S* or *X* bands in our VLA follow-up observations.

We found a hard X-ray spectrum with three Fe lines. This is fit well with a `mkcflow` spectral model with an additional Gaussian line for neutral Fe, which is doubly absorbed by local and ISM material. We find H_α and He lines in the optical/IR spectra, the former of which are double-peaked and evolves with time.

In our timing analysis we found two periods, at 449.7 s and 459.89 s, which we interpret to be the spin and beat periods of an IP magnetic CV system. From these periods we infer an orbital period of 5.6 hr. This orbital period is consistent with periods seen with moderate significance in two independent data sets of long-baseline optical photometry (ZTF and SAAO). The orbital, spin, and beat period detections provide strong evidence of an IP classification for J1839. Other supporting evidence includes the complex nature of the optical emission lines and the presence of He II 4686 Å emission. Furthermore, we find a sinusoidal pulse profile in the X-ray data at the spin period, with a pulse fraction that decreases with increasing energy, another characteristic that supports the IP origin of J1839.

The authors wish to thank Sylvia Rose Kowalski and Deena Mickelson for their roles in VLA data acquisition. They also thank Hannes Breytenbach for taking some of the SAAO data. P.A.W. acknowledges financial support from the University of Cape Town and the National Research Foundation. The SALT observations reported here were obtained through the SALT Large Science program 2018-2-LSP-001, with D.B. as PI, who also acknowledges support of the National Research Foundation. C.K. and N.G. acknowledge support under NASA grant 80NSSC19K0916 and Smithsonian Astrophysical Observatory grant GO9-20057X. B.O. is supported in part by the National Aeronautics and Space Administration through grants NNX16AB66G, NNX17AB18G, and 80NSSC20K0389.

We thank the NRAO for the generous allocation of VLA time for our observations. The National Radio Astronomy Observatory is a facility of the National Science Foundation operated under cooperative agreement by Associated Universities, Inc.

This work has made use of data from the European Space Agency mission Gaia, processed by the Gaia Data Processing and Analysis Consortium (DPAC, https://www.cosmos.esa.int/web/gaia/dpac/consortium). Funding for the DPAC has been provided by national institutions participating in the Gaia Multilateral Agreement.

Facilities: Swift, NuSTAR, XMM-Newton, Chandra, SALT, SAAO, Gaia, Pan-STARRS, ZTF, APO, VLA.

Software: casa (McMullin et al. 2007), heasoft (v6.23; Nasa High Energy Astrophysics Science Archive Research Center (Heasarc), 2014), ds9 (Joye & Mandel 2003; Smithsonian Astrophysical Observatory 2000), sas (v1.2; Gabriel et al. 2004), pyspeckit (Ginsburg & Mirocha 2011), stingray (Huppenkothen et al. 2019, v0.1;), ciao (Fruscione et al. 2006, v4.9;), pydis (Davenport 2019), pysalt package (Crawford et al. 2010), python 3 (Van Rossum & Drake 2009), iraf (Tody 1986, 1993), vartools (Hartman & Bakos 2016)

ORCID iDs

Nicholas M. Gorgone https://orcid.org/0000-0002-1653-6411
Patrick A. Woudt https://orcid.org/0000-0002-6896-1655
David Buckley https://orcid.org/0000-0002-7004-9956
Koji Mukai https://orcid.org/0000-0002-8286-8094
Chryssa Kouveliotou https://orcid.org/0000-0003-1443-593X
Daniela Huppenkothen https://orcid.org/0000-0002-1169-7486
Ersin Göğüş https://orcid.org/0000-0002-5274-6790
Eric Bellm https://orcid.org/0000-0001-8018-5348
Justin D. Linford https://orcid.org/0000-0002-3873-5497
Alexander J. van der Horst https://orcid.org/0000-0001-9149-6707
Matthew G. Baring https://orcid.org/0000-0003-4433-1365
Dieter Hartmann https://orcid.org/0000-0002-8028-0991
Paul Barrett https://orcid.org/0000-0002-8456-1424
Melissa Graham https://orcid.org/0000-0002-9154-3136
Jamie Kennea https://orcid.org/0000-0002-6745-4790
Brendan M. O'Connor https://orcid.org/0000-0002-9700-0036
Daniel Stern https://orcid.org/0000-0003-2686-9241
Patrick Slane https://orcid.org/0000-0002-6986-6756
Ralph Wijers https://orcid.org/0000-0002-3101-1808

References

Abril, J., Schmidtobreick, L., Ederoclite, A., & López-Sanjuan, C. 2020, MNRAS, 492, L40
An, H., Madsen, K. K., Westergaard, N. J., et al. 2014, Proc. SPIE, 9144, 91441Q
Bailer-Jones, C. A. L., Rybizki, J., Fouesneau, M., Mantelet, G., & Andrae, R. 2018, AJ, 156, 58
Bayo, A., Rodrigo, C., Barrado Y Navascués, D., et al. 2008, A&A, 492, 277
Beuermann, K., Burwitz, V., Reinsch, K., Schwope, A., & Thomas, H. C. 2021, A&A, 645, A56
Bildsten, L., Chakrabarty, D., Chiu, J., et al. 1997, ApJS, 113, 367
Britt, C. T., Maccarone, T., Pretorius, M. L., et al. 2015, MNRAS, 448, 3455
Buccheri, R., Bennett, K., Bignami, G. F., et al. 1983, A&A, 128, 245
Buckley, D. A. H., Swart, G. P., & Meiring, J. G. 2006, Proc. SPIE, 6267, 62670Z
Burgh, E. B., Nordsieck, K. H., Kobulnicky, H. A., et al. 2003, Proc. SPIE, 4841, 1463
Chambers, K. C., Magnier, E. A., Metcalfe, N., et al. 2016, arXiv:1612.05560
Coppejans, D. 2016, PhD thesis, Radboud Univ. Nijmegen
Coppejans, D. L., Woudt, P. A., Warner, B., et al. 2014, MNRAS, 437, 510
Coppejans, R., Gulbis, A. A. S., Kotze, M. M., et al. 2013, PASP, 125, 976
Crawford, S. M., Still, M., Schellart, P., et al. 2010, Proc. SPIE, 7737, 773725
Cropper, M. 1990, SSRv, 54, 195
Davenport, J. R. A. 2019, PyDIS, https://github.com/TheAstroFactory/pydis
de Martino, D., Bernardini, F., Mukai, K., Falanga, M., & Masetti, N. 2020, AdSpR, 66, 1209
Done, C., & Magdziarz, P. 1998, MNRAS, 298, 737
Evans, P. A., Osborne, J. P., Beardmore, A. P., et al. 2014, ApJS, 210, 8
Ezuka, H., & Ishida, M. 1999, ApJS, 120, 277
Fruscione, A., McDowell, J. C., Allen, G. E., et al. 2006, Proc. SPIE, 6270, 62701V
Gaia Collaboration, Brown, A. G. A., Vallenari, A., et al. 2018, A&A, 616, A1
Gabriel, C., Denby, M., Fyfe, D. J., et al. 2004, in ASP Conf. Ser. 314, Astronomical Data Analysis Software and Systems (ADASS) XIII, ed. F. Ochsenbein, M. G. Allen, & D. Egret (San Francisco, CA: ASP), 759
Ginsburg, A., & Mirocha, J. 2011, PySpecKit: Python Spectroscopic Toolkit, ascl:1109.001
Gorgone, N., & Kouveliotou, C. 2017, AAS Meeting, 16, 105.22
Hartman, J. D., & Bakos, G. Á 2016, A&C, 17, 1
Hellier, C. 1997, MNRAS, 291, 71
Hellier, C., & Mukai, K. 2004, MNRAS, 352, 1037
Hellier, C., Mukai, K., & Osborne, J. P. 1998, MNRAS, 297, 526
Huppenkothen, D., Bachetti, M., Stevens, A. L., et al. 2019, ApJ, 881, 39
Joye, W. A., & Mandel, E. 2003, in ASP Conf. Ser. 295, Astronomical Data Analysis Software and Systems XII, ed. H. E. Payne, R. I. Jedrzejewski, & R. N. Hook (San Francisco, CA: ASP), 489
Lallement, R., Babusiaux, C., Vergely, J. L., et al. 2019, A&A, 625, A135
Littlefield, C., Garnavich, P., Kennedy, M. R., et al. 2016, ApJ, 833, 93
Lopes de Oliveira, R., & Mukai, K. 2019, ApJ, 880, 128
Madsen, K. K., Grefenstette, B. W., Pike, S., et al. 2020, arXiv:2005.00569
Masci, F. J., Laher, R. R., Rusholme, B., et al. 2019, PASP, 131, 018003
McClintock, J. E., Canizares, C. R., & Tarter, C. B. 1975, ApJ, 198, 641
McMullin, J. P., Waters, B., Schiebel, D., Young, W., & Golap, K. 2007, in ASP Conf. Ser. 376, Astronomical Data Analysis Software and Systems XVI, ed. R. A. Shaw, F. Hill, & D. J. Bell (San Francisco, CA: ASP), 127
Mukai, K. 2017, PASP, 129, 062001
Mukai, K., & Shiokawa, K. 1993, ApJ, 418, 863
NASA High Energy Astrophysics Science Archive Research Center (Heasarc) 2014, HEAsoft: Unified Release of FTOOLS and XANADU, ascl:1408.004
Pala, A. F., Gänsicke, B. T., Breedt, E., et al. 2020, MNRAS, 494, 3799
Patterson, J. 1994, PASP, 106, 209
Potter, S. B., Buckley, D. A. H., O'Donoghue, D., et al. 2010, MNRAS, 402, 1161
Pretorius, M. L. 2009, MNRAS, 395, 386
Pretorius, M. L., & Mukai, K. 2014, MNRAS, 442, 2580
Smithsonian Astrophysical Observatory 2000, SAOImage DS9: A utility for displaying astronomical images in the X11 window environment, ascl:0003.002
Tody, D. 1986, Proc. SPIE, 627, 733
Tody, D. 1993, in ASP Conf. Ser. 52, Astronomical Data Analysis Software and Systems II, ed. R. J. Hanisch, R. J. V. Brissenden, & J. Barnes (San Francisco, CA: ASP), 173
Van Rossum, G., & Drake, F. L. 2009, Python 3 Ref. Manual (Scotts Valley, CA: CreateSpace)
Warner, B. 1986, MNRAS, 219, 347
Warner, B. 1992, in ASP Conf. Ser. 29, Cataclysmic Variable Stars, ed. N. Vogt (San Francisco, CA: ASP), 242
Warner, B. 1995, Cataclysmic Variable Stars (Cambridge: Cambridge Univ. Press)
Wickramasinghe, D. 2014, in European Physical Journal Web of Conf. 64, Physics at the Magnetospheric Boundary, ed. E. Bozzo et al. (Paris: EDP Sciences), 03001